Co-published by
Institute of Fluid-Flow Machinery
Polish Academy of Sciences
Committee on Thermodynamics and Combustion
Polish Academy of Sciences

http://www.imp.gda.pl/archives-of-thermodynamics/

Understanding of RANS-modelled impinging jet heat transfer trough turbulence kinetic energy, momentum and energy budgets

Sebastian Gurgul[a], Elzbieta Fornalik-Wajs[a*]

[a]AGH University of Krakow, Al. Mickiewicza 30, Krakow 30-059, Poland
*Corresponding author email: elzbieta.fornalik@agh.edu.pl

Received: 09-05-2024; revised: 20-06-2024; accepted: 21-06-2024

Abstract

Impinging jets are one of the most effective techniques of heat transfer intensification, therefore they are continuously applied in various engineering areas. On the other hand, a numerical modelling of complex phenomena contributing to an overall heat transfer effect (and the Nusselt number value) is still not sufficient and suffers from lack of generalization. The extensive studies have been conducted to unify approach to the impinging jet modelling and construct the model (in Ansys Fluent software), which allows mirroring of the results. Presented work discusses differences in representation of impinging jet between various turbulence models based on the turbulence kinetic energy, momentum and energy budgets. It allows deep understanding of influence of geometrical and flow parameters on fluid mechanics phenomena interaction and final effect. The most significant results are connected with linking of Nusselt number distribution with analyzed budgets' terms. Each term contributes to the distribution and cannot be omitted. Drawn conclusions explain the origin of reported in literature differences and includes suggestions, how to evaluate the Nusselt number distribution results coming from various turbulence models. At this stage of research to have a complete image of relation between the particular quantities budgets and heat transfer effect it is suggested to consider also the turbulence kinetic energy dissipation budget, which will fil opened by this research gap.

Keywords: Round impinging jet; Turbulence kinetic energy budget; Momentum budget; Energy budget; Nusselt number

Vol. 45(2024), No. 3, 13–30; doi: 10.24425/ather.2024.150451

Cite this manuscript as: Gurgul, S., & Fornalik-Wajs, E. (2024). Understanding of RANS-modelled impinging jet heat transfer trough turbulence kinetic energy, momentum and energy budgets. *Archives of Thermodynamic*s, 45(3), 13–30.

1. Introduction

Turbulent round jet impingement has been studied for a long time. However, due to its complexity and high heat transfer performance, this phenomenon still attracts the attention of researchers and is a subject of both numerical and experimental studies [1]. The description of this process is influenced by various factors such as the Reynolds number, the Prandtl number, the nozzle-to-impingement-plate distance ratio (H/D), the nozzle shape, the inlet velocity profile, and many others [1–4], whose make it challenging to compare the results from different studies [5]. Numerical analysis of jet impingement can be carried out using direct numerical simulation (DNS), large eddy simulation (LES), or Reynolds averaged Navier-Stokes (RANS) approach. The first two methods provide insight into the physics of the process but are computationally expensive compared to

Nomenclature

C_P – specific heat capacity, J/(kg K)
D – inlet diameter, m
f – elliptic relaxation function
H – nozzle-to-impingement-plate-distance, computational domain height, m
H/D – nozzle-to-impingement-plate-distance to inlet diameter ratio
k – turbulence kinetic energy, m^2/s^2
Nu – Nusselt number
P – average pressure, Pa
Pr – Prandtl number
$\dot{q}$ – wall heat flux, W/m^2
Re – Reynolds number
S – strain rate tensor, 1/s
T – average temperature, K
T_{in} – reference inlet temperature, K
T_w – local wall temperature, K
$\overline{u_i u_j}$ – Reynolds stress term, m^2/s^2
U – average radial velocity, m/s
$|U|$ – average inlet velocity, m/s
U_i, U_j – average velocity components, m/s
$\overline{v^2}$ – velocity fluctuation
V – average axial velocity, m/s
x – radial coordinate, m
x_i, x_j – Cartesian coordinates, m
x/D – radial coordinate to inlet diameter ratio
y – axial coordinate, m
$y+$ – dimensionless distance from the wall

Greek symbols

α – heat transfer coefficient, W/(m^{2}K)
α_k – inverse effective Prandtl number
β^* – model constant
γ – intermittency
ε – turbulence dissipation rate, m^2/s^3
λ – thermal conductivity, W/(m K)
μ – dynamic viscosity, Pa s
μ_{eff} – effective viscosity, Pa s
μ_t – turbulent viscosity, Pa s
$\overline{u_j\theta}$ – turbulent heat flux, Km/s
ρ – density, kg/m^3
σ_k, σ_t – turbulent Prandtl number
ω – specific turbulent dissipation rate, 1/s
Ω – magnitude of the vorticity rate, 1/s

Subscripts and Superscripts

E – energy equation
k – turbulence kinetic energy equation
M – momentum equation

Abbreviations and Acronyms

CONV – convection term
DIFF – diffusion term
DISS – dissipation term
DNS – direct numerical simulation
LES – large eddy simulation
PRESS – pressure term
PROD – production term
RANS – Reynolds averaged Navier-Stokes
RNG – renormalisation group
RS – Reynolds stress term
SST – shear stress transport
TDIFF – turbulent diffusion term
TKE – turbulence kinetic energy
UDF – user-defined function

the last one [1]. The third method is more suitable from an engineering perspective, where turbulent flow is more common, and it is a valuable tool for analyzing and predicting heat transfer performance [1]. Despite many research efforts in this field, there are still discrepancies in predicting the local Nusselt number distribution numerically, especially in the position of its secondary maximum [6,7].

According to Kořínek et al. [8], the resolution of near-wall mesh significantly affected the heat transfer of the round jet impingement when using scale-resolving-simulation methods. They found that mesh refinement in the longitudinal direction is more crucial than in the perpendicular direction. Furthermore, they observed that grid refinement was particularly beneficial for LES and DES (detached eddy simulation) calculations when dealing with cases of low nozzle-to-plate distance. The paper by Domino and Wenzel [9] described the results of DNS calculations for a series of non-isothermal turbulent impinging jet configurations. The simulations showed an increase in radial mixing as the jet temperature increased. Regions of large negative production of turbulence kinetic energy were noted to be a function of the difference between the axial and radial normal stresses, with crucial inflection points occurring where their magnitudes changed. A large recirculation structure was evident in all simulations, highlighting a faster mixing of nest-like structures at the higher nozzle-to-impingement-plate-distance ratio. Magagnato et al. [4] conducted DNS calculations to examine the impact of the Prandtl number on the heat transfer of a circular impinging jet. In this study, the temperature field was considered as a passive scalar. The study confirmed that the Prandtl number affects the value of the Nusselt number at a fixed Reynolds number. The distribution of the Nusselt number along the plate exhibited similar features at different Prandtl numbers and showed a characteristic secondary maximum for both analyzed Reynolds numbers (5 300 and 10 000) at Pr = 0.025 and Pr = 0.01. Huang et al. [10] developed a turbulence model for jet impingement heat transfer based on the k–ω SST (shear stress transport) turbulence model, which considered the effects of the cross-diffusion term and the Kato-Launder model. The modified model agreed well with the cases studied and overcame the false sec-

ondary Nusselt number maximum (not observed in the experimental studies) at a high nozzle-plate spacing for slot jets, which the standard k–ω SST turbulence model predicted. The study indicated that the pressure gradient played an essential role in turbulent slot impinging jet, and the effect of the cross-diffusion term should be taken into account in the boundary layer. Developed shear stress transport (SST) model was used by Zhang et al. [11] to simulate turbulent round jet impingement heat transfer. The model included an additional switching function for cross-diffusion correction, which provided accurate results in terms of heat transfer by capturing the closest first maximum, local minimum, and secondary maximum compared to other models, except for problems at low nozzle-plate spacing. The inner maximum at the stagnation point was linked to the radial pressure gradient, Therefore reinforcing sensitivity to pressure in a turbulence model can help to improve the prediction of heat transfer characteristics. The paper by Huang et al. [12] discussed a modification of the k–ω SST model for swirling impinging jets, specifically the SST model with curvature correction (SSTCC) and the modified SST model using the cross-diffusion term (SSTCD). They noticed that the SSTCC model might falsely enhance the effect of swirl/streamline curvature compared to the experimental results. However, the effect of curvature correction could be ignored downstream, leading to a similar performance of the SSTCC and SST models. The authors concluded that the SSTCD model significantly improves the SST model to predict heat transfer in the flows demonstrated in the paper. Menzler et al. [6] evaluated the Ansys GEKO turbulence model for its ability to determine the local and integral Nusselt number of an impinging jet. The GEKO (generalized k-ω) turbulence model has some parameters that can be adjusted. The authors achieved an accuracy of about 10% in the prediction of the local Nusselt number, while adjusting those parameters, but the limits of the recommended parameters were exceeded. The study by Chitsazan et al. [2] presented the results of numerical simulations of a single impinging round jet using different numerical parameters. The researchers compared the results of different implementations of the k–ω SST model, identifying the low Reynolds number damping modification (correction of turbulent viscosity) as essential to predict the secondary maximum. The study was concluded that good results could be achieved with a coarse grid if the boundary region is resolved adequately. Moreover, polyhedral grids lead to good quality results with lower memory requirements, cell numbers, and shorter run times than other cell shapes. The quality of results obtained for various shapes of the elements was similar to that of polyhedral grids. Huang et al. [13] investigated the effects of roughness on heat transfer and flow structures for round jet impingement using the shear stress transport model with the transition model. The study showed that roughness enhanced heat transfer by 2.53% to 6.08% compared to a smooth surface, but this enhancement is nonmonotonic due to changes in the secondary maximum of heat transfer. Increasing roughness height enhanced turbulent intensity and led to an early occurrence of the secondary heat transfer maximum, which is crucial for heat transfer augmentation. Kaewbumrung and Plengsa-Ard [14] examined a single air jet impingement at a constant temperature, employing different RANS turbulence models ($\overline{v^2} - f$ and four Reynolds stress turbulence models) to compare with published measurement data. The focus was on the secondary maximum of the Nusselt number, which was clearly generated using the ratio of H/D = 2. The $\overline{v^2} - f$ model was found to have better numerical precision in analysis of the local Nusselt number and velocity profiles. The first maximum of the Nusselt number location was observed at 0.5 diameter from stagnation point (x/D) due to the change in the radial flow velocity, while a secondary maximum was observed at a radial distance of approximately x/D = 2.05. The study by Siddique et al. [15] aimed to predict the flow pattern and determine the local value of the Nusselt number for varying heat flux input boundary conditions. The research based on the SST + Gamma-Theta turbulence model, successfully captured the turbulence phenomenon of intermittency, flow separation, local velocity gradient, and transition. The findings suggested that the Nusselt number is the least affected by the nozzle-target spacing in the stagnation region because the velocity gradient development was dominated by an impinging jet momentum. However, the development of the velocity gradient on the target surface dominated after the stagnation region. Finally, the dependency of the nozzle-target spacing caused a more significant impact under constant heat flux boundary conditions as a result of the further development of a thermal boundary layer. The experimental study by Kumar et al. [16] referred to the heat transfer characteristics of a free-surface single-phase circular liquid jet impinging on a smooth, flat surface under varying nozzle diameter, nozzle-to-plate spacing, and Reynolds number. The results revealed that the local Nusselt number reached maximum in the stagnation region and decreased downstream. The Nusselt number was found to be a function of the Reynolds number, the Prandtl number, system length, and the Weber number. Comparison of a free surface and a submerged jet exhibited that the heat transfer rate was higher in the case of a submerged jet. Some recent review publications have collected research in various areas of the jet impingement, such as the influence of target surface shape and geometry configuration [1,17], excited jets [17], nanofluids [17–19], single jet impingement [1,19], jet arrays [1,19], swirling jet impingement [19] and synthetic jets [19].

The literature overview reveals a focus on improving heat transfer prediction through the modification or development of existing turbulence models. Additionally, there has been an increase in the number of publications that present DNS analysis, which can provide valuable insight into jet impingement flow and heat transfer physics. Other investigations aimed to enhance heat transfer using various working fluids or target surfaces. In addition to numerous numerical investigations, new experimental studies emerged. According to Barbosa et al. [1], the behavior of geometric and flow parameters in the jet impingement is well understood, but their interactions are complex. Recent studies on the numerical simulation of jet impingement have mainly concentrated on a single jets. The choice of turbulence model plays a crucial role, and based on various studies, the k–ω SST turbulence model has been identified as a reliable and efficient option for accurate modeling of jet impingement while minimizing computing time.

Despite extensive numerical research, it remains challenging to find studies in the literature that attempt to identify, describe, and explain the sources of differences in the heat transfer behavior of various turbulence models. Before modification and development of turbulence models, it is crucial to conduct an analysis that provides a deeper understanding of the physics behind commonly used turbulence models. Such an analysis can be based on turbulence kinetic energy (TKE), momentum, and energy budgets, and it gives valuable insights into the characteristics of these models.

The literature contains several publications that focus on the transport equations and analysis of TKE, which can be broadly classified into two groups. The first group includes studies that rely on DNS and experimental methods, while the second group comprises budgets obtained through RANS calculations. In a DNS study by Domino and Wenzel [9], the TKE values were calculated on the surfaces parallel to the impinged one at three different inlet temperature values. The authors observed that the TKE values increased with increasing inlet temperature, with the maximum value found at $x/D \approx 0.5$. Negative TKE production was noted near the impinged surface at values of $x/D < 6$. The study also showed that the sign of TKE production changed when the axial component of the Reynolds stress surpassed the radial one. An experimental study by Alekseenko et al. [3] was related to a budget of axial momentum and TKE on lines parallel to the impinged surface for conventional and swirling jets. For the momentum budget, the study showed that the viscous term was negligible compared to other terms, and convection was characterized by an almost constant positive value near the jet axis. For the TKE budget, the viscous term, the same as for momentum, was negligible. Maximum magnitudes of dissipation, diffusion of pressure and shear stress production were observed near $x/D \approx 0.5$, corresponding to the region of the mixing layer. The convection term and turbulent diffusion possessed opposite signs, and the production term had local maxima in the mixing regions for all analyzed cases. In two publications by Ries et al. [20,21], DNS numerical analysis and PIV (particle image velocimetry) experimental study were presented. They studied jet impingement on inclined surfaces at 0°, 45° and 90°. The production of TKE was negative in the vicinity of the wall in the stagnation region, and was balanced by pressure-related diffusion rather than viscous dissipation. Molecular and pressure-related diffusion dominated, while dissipation was relatively small. In an experimental study conducted by Nishino et al. [22], the TKE budget was presented. The study exhibited that the negative TKE production occurred near the wall and was compensated by pressure diffusion.

The analysis of TKE, the budget of TKE, and the momentum calculated on the basis of the RANS results can be found in four publications by Kura et al. In the first paper [23], the authors presented the TKE values in two parallel lines: one at the impinged wall and another outside the boundary layer. They noted that only the values inside the boundary layer are meaningful. The TKE values were then compared with the distribution of the local Nusselt number, where inflection points were observed at nearly the exact locations of the Nusselt number maxima. In the second paper [24], the TKE budget obtained by $\zeta - f$ turbulence model was presented to show the difference between various impinged surfaces such as flat, convex, and concave. Additionally, a comparison between momentum budgets by $\zeta - f$ and $\overline{v^2} - f$ turbulence models was presented. In the case of the TKE budget, the authors concluded that the overall trend is the same for all types of surfaces, but the only differences refer to the maximal values and their positions. The momentum budget was prepared on two lines perpendicular to the impinged surface, the first being located at the stagnation zone that begins to decay, and the further where the second Nusselt maximum occurs. The $\overline{v^2} - f$ turbulence model was characterized by a significantly higher momentum diffusion near the wall than the $\zeta - f$ turbulence model. The third investigation [25] compared TKE production and dissipation between different types of target surfaces. The general conclusion was that the tendency was similar, but the highest TKE production was observed in the stagnation zone for the convex case. The last investigation [26] presented a comparison between the TKE budget for two different inlet conditions. Regarding the budget, the authors showed that diffusion and dissipation dominated production and convection ones. The convective term possessed a negative value near the stagnation point and changed its sign near the location of the Nusselt number secondary maxima occurrence. The link between the values and trends of TKE and Nusselt number were pointed out.

Numerical investigations such as the DNS and experimental studies are priceless for understanding the physics of jet impingement, but they are expensive and time-consuming. On the other hand, analysis of the TKE and transport equations based on the RANS calculations may only partially explain this phenomenon, because they are just the models. However, such an analysis can still help to identify why various turbulence models lead to a different tendency of the results in simulating jet impingement and to modify and further develop the RANS turbulence models. Unfortunately, finding a comparative and complex analysis of various turbulence models in the literature that describes and explains the sources of discrepancies in heat transfer results is challenging. There are very few comprehensive analyses, which enable configuration of the numerical model. Therefore, the authors decided to present their research, which fills the gap and meets the need of the readers.

The previous research [27] considered the heat transfer of classic jet impingement. In the numerical studies, 80 different cases were investigated, which included five different turbulence models (k–ε RNG Kato-Launder, k–ω SST Kato-Launder, intermittency transition, transition SST, and $\overline{v^2} - f$), four geometrical configurations described by the dimensionless ratio of H/D (where H is the computational domain height, D is the inlet diameter) such as H/D = 1, 2, 4 and 6, and 4 hydrodynamic parameters defined by the Reynolds number (Re = 10 000, 20 000, 23 000 and 30 000),

$$\mathrm{Re} = \frac{\rho |U| D}{\mu}, \tag{1}$$

where: ρ is the fluid density; $|U|$ is the average inlet velocity, D is the inlet diameter, and μ is the fluid dynamic viscosity.

The study produced valuable findings, including the 80 distributions of local Nusselt number along the heated wall. The local Nusselt number was defined as follows:

$$\mathrm{Nu} = \frac{\alpha D}{\lambda}, \tag{2}$$

$$\alpha = \frac{\dot{q}}{T_w - T_{in}}, \tag{3}$$

where: α is the heat transfer coefficient, D is the inlet diameter, λ is the fluid thermal conductivity, $\dot{q}$ is the wall heat flux, T_w is the local wall temperature, and T_{in} is the reference inlet temperature.

Based on the previous analysis [27], the authors could compare various turbulence models and investigate their features under various geometrical and hydrodynamical conditions and presented systematic analyses with precise definitions of numerical model settings and comparisons with numerous experimental and numerical studies. As a result of the research, three turbulence models, which are the k–ε RNG Kato-Launder, k–ω SST Kato-Launder, and the Intermittency transition model, have been selected. This paper is an extension of previous studies towards the TKE values. Analyses were conducted for the three above-mentioned turbulence models and two geometrical configurations with presentation of the TKE, momentum, and energy budgets. The results are compared with the local Nusselt number distribution. They lead to explanation of differences between turbulence models prediction of heat transfer and formulation of the guidelines for selection of turbulence model suitable for particular research problem. An additional benefit of presented studies is a transparent and easy-to-be reproduced numerical model. It is worth to mention that listing of own function used to calculate diffusion term of momentum and energy equations is included.

2. Mathematical model, geometry, and boundary conditions

Figure 1 shows the geometry and boundary conditions of the 2D axisymmetric model. The justification of the 2D axisymmetric model was based on the numerical analysis of 3D and 2D geometries presented in [27]. In this model, air at a constant temperature of 293 K and a fully developed profile enters the computational domain through the inlet channel. After forming a jet, the air impinged on the bottom wall (heated with a constant heat flux of 1000 W/m^2), then creates a wall jet along the heated surface and escapes the computational domain via the right surface. The air used in the analysis was considered as Newtonian, incompressible fluid with constant thermophysical properties (ρ = 1.225 kg/m^3, C_P = 1006.43 J/(kg K), λ = 0.0242 W/(m K), μ = 1.7894×10^{-5} Pa s). The steady-state analysis involved three transport equations, mass, momentum, and energy [28]:

$$\frac{\partial U_j}{\partial x_j} = 0, \tag{4}$$

$$\rho \frac{\partial (U_i U_j)}{\partial x_j} = -\frac{\partial P}{\partial x_i} + \frac{\partial}{\partial x_j}\left[\mu\left(\frac{\partial U_i}{\partial x_j} + \frac{\partial U_j}{\partial x_i}\right) - \rho\overline{u_i u_j}\right], \tag{5}$$

$$\rho \frac{\partial (U_j T)}{\partial x_j} = \frac{\partial}{\partial x_j}\left(\frac{\lambda}{C_P}\frac{\partial T}{\partial x_j} - \rho\overline{u_j \theta}\right), \tag{6}$$

where: U_i, U_j are the average velocity components, x_i, x_j are the Cartesian coordinates, ρ is the density, P is the average pressure, μ is the dynamic viscosity, $\overline{u_i u_j}$ is the Reynolds stress term, calculated by the Boussinesq hypothesis, T is the average temperature, λ is the thermal conductivity, C_P is specific heat capacity, $\overline{u_j \theta}$ is the turbulent heat flux.

Additionally, RANS equations such as turbulence kinetic energy k, turbulent dissipation rate ε, specific turbulent dissipation rate ω and intermittency γ were incorporated for turbulence modeling [28]. To ensure accuracy, a block-structured mesh was prepared for each geometrical configuration, and y+ was kept equal to or below 1. The y+ value is a dimensionless parameter that represents the distance from the first grid cell to the surface wall. The total cell number for the first geometrical configuration (H/D = 2) was equal to 63 100, and for the second (H/D = 6) it was 68 600 cells. Both meshes have passed the grid independence test. The discretization of the second geometrical case is presented in Fig. 2.

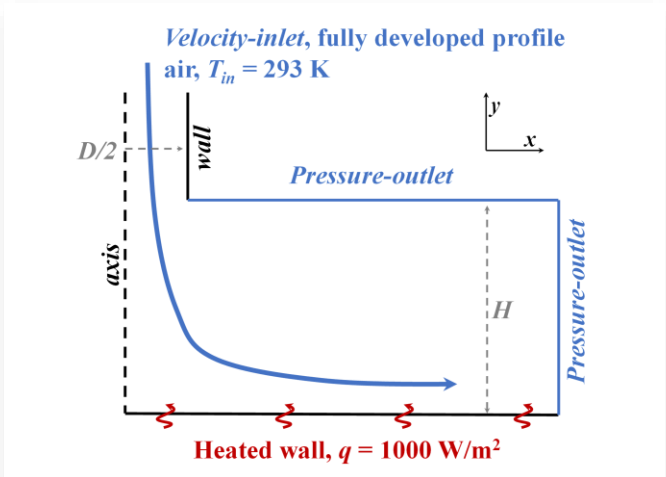

Fig. 1. Geometry and boundary conditions. Inlet diameter D = 0.02 m.

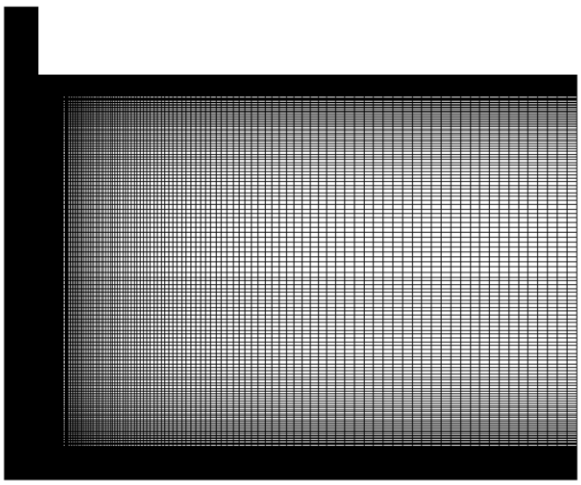

Fig. 2. Mesh for H/D = 6, D = 0.02 m, $y^+ < 1$, and total cell number = 68 600.

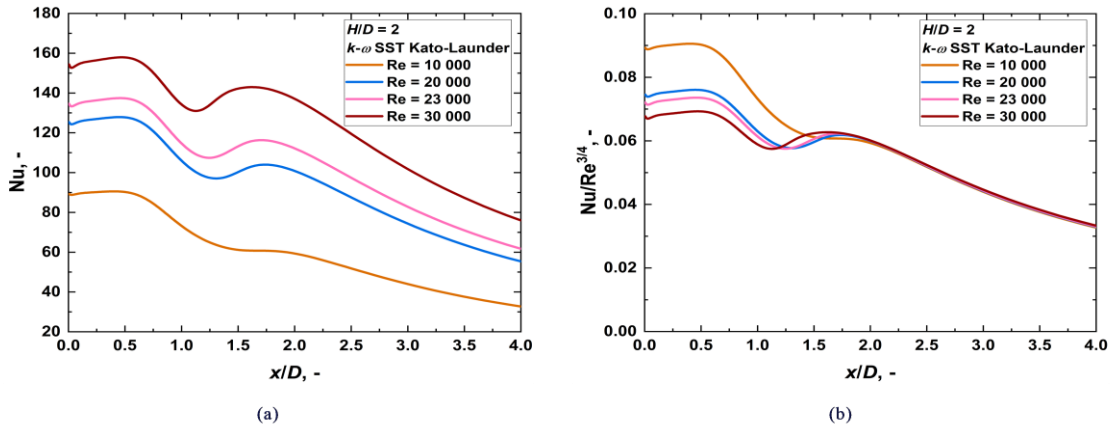

Fig. 3. (a) Local Nusselt number distribution. (b) Normalized local Nusselt number distribution. k–ω SST Kato-Launder turbulence model, H/D = 2.

The numerical calculations were performed in Ansys Fluent 18.1, where the pressure-based solver with SIMPLE (Semi-Implicit Method for Pressure Linked Equations) algorithm was used. The second-order numerical scheme was chosen for the pressure, momentum, turbulence, and energy equations. The insight of the mesh and detailed description of the numerical procedure can be found in the previous publication [27]. The model validation presented in this publication included a comparison of 16 turbulence models with 11 different experimental analyses. All source data are stored in the open repository [29].

Figure 3 presents the local Nusselt number distribution along the heated wall for different Reynolds number values and one geometrical configuration (H/D = 2). The purpose of this figure is to demonstrate that for the same geometrical configuration, the Nusselt number distribution does not vary significantly with different Reynolds numbers, which is particularly evident for normalized Nusselt number which is defined as Nu/Re^m. In the literature, the scaling factor for the Nusselt number is typically set to be $Nu/Re^{2/3}$ [1,11,30], but the exponent m can vary between 0.55 and 0.87 for a single jet impingement [1]. At values of x/D greater than 2.0, no differences in the Nusselt number distribution are observed at various Reynolds numbers which is especially very clear when the scaling factor is equal to $Nu/Re^{3/4}$ (Fig. 3(b)). However, near the stagnation point (x/D < 2.0), some discrepancies are visible, primarily due to variations in the inlet profile, which significantly affects the local Nusselt number distribution in that region. Furthermore, comparing the local Nusselt number distribution for geometrical configuration (H/D = 2 and 6) at the same Reynolds number in Fig. 4 reveals different trends, especially at various H/D. Two particular trends of the Nusselt number distribution can be distinguished depending on the H/D parameter [2,4,7,10,11,31,32]. At H/D < 6.0 (confirmed in [27]), there is a characteristic secondary maximum in the Nusselt number distribution. In contrast, at higher values of H/D, the second Nusselt number maximum does not occur (some turbulence models may exhibit an artificial/false secondary Nusselt number maximum, which is not observed in experimental studies [10,27]). Therefore, in this publication, the authors will compare the results of two H/D values at a constant Reynolds number of 23 000. Based on the literature and previous studies the authors have selected three turbulence models which are most appropriate for modeling the jet impingement phenomenon. These models will also be used for the comparison of results.

In the presented study, the analysis is focused on the Reynolds number equal to 23 000, two different configurations (H/D = 2 and 6), and three previously selected turbulence models (k–ε RNG Kato-Launder, k–ω SST Kato-Launder, intermittency transition). The primary objective of this analysis is to demonstrate the differences between turbulence models concerning low (H/D = 2) and high (H/D = 6) geometrical configurations and to provide valuable insights into the turbulence modeling of round jet impingement.

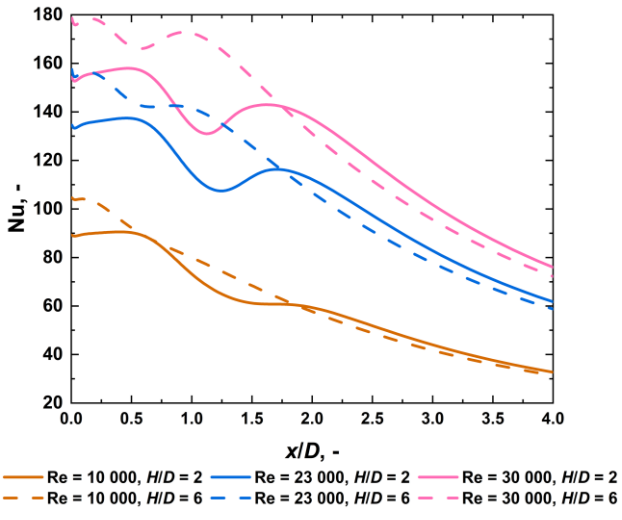

Fig. 4. Comparison of local Nusselt number distribution at heated wall, between different values of H/D and Reynolds number. k–ω SST Kato-Launder turbulence model.

3. The budgets

To conduct a comparative study, the authors utilize the values of k (turbulence kinetic energy, TKE) and budget of TKE, axial

Table 1. The turbulence kinetic energy equation terms [28].

Term	*k–ε* RNG Kato-Launder	*k–ω* SST Kato-Launder	Intermittency transition
Convection	$\rho\left(U\frac{\partial k}{\partial x}+V\frac{\partial k}{\partial y}\right)$		
Production	$\min(\mu_t S\Omega, 10\rho\varepsilon)$	$\min(\mu_t S\Omega, 10\rho\beta^* k\omega)$	$\gamma\min(\mu_t S\Omega, 10\rho\beta^* k\omega)$
Dissipation	$\rho\varepsilon$	$\rho\beta^* k\omega$	$\min(\max(\gamma, 0.1), 1.0)\rho\beta^* k\omega$
Diffusion	$\frac{\partial}{\partial x}\left(\alpha_k\mu_{eff}\frac{\partial k}{\partial x}\right)+\frac{\partial}{\partial y}\left(\alpha_k\mu_{eff}\frac{\partial k}{\partial y}\right)$	$\frac{\partial}{\partial x}\left(\left(\mu+\frac{\mu_t}{\sigma_k}\right)\frac{\partial k}{\partial x}\right)+\frac{\partial}{\partial y}\left(\left(\mu+\frac{\mu_t}{\sigma_k}\right)\frac{\partial k}{\partial y}\right)$	$\frac{\partial}{\partial x}\left(\left(\mu+\frac{\mu_t}{\sigma_k}\right)\frac{\partial k}{\partial x}\right)+\frac{\partial}{\partial y}\left(\left(\mu+\frac{\mu_t}{\sigma_k}\right)\frac{\partial k}{\partial y}\right)$

where: ρ is the density, g/m^3; k is the turbulence kinetic energy, m^2/s^2; U is the average radial velocity, m/s; V is the average axial velocity, m/s; x is the radial coordinate, m; y is the axial coordinate, m; μ is the dynamic viscosity, Pa·s; μ_t is the turbulent viscosity, Pa·s; $S=\begin{bmatrix}\frac{\partial U}{\partial x} & \frac{1}{2}\left(\frac{\partial U}{\partial y}+\frac{\partial V}{\partial x}\right)\\ \frac{1}{2}\left(\frac{\partial V}{\partial x}+\frac{\partial U}{\partial y}\right) & \frac{\partial V}{\partial y}\end{bmatrix}$ is the strain rate tensor, 1/s; $\Omega=\begin{bmatrix}0 & \frac{1}{2}\left(\frac{\partial U}{\partial y}-\frac{\partial V}{\partial x}\right)\\ \frac{1}{2}\left(\frac{\partial V}{\partial x}-\frac{\partial U}{\partial y}\right) & 0\end{bmatrix}$ is the magnitude of the vorticity rate, 1/s; ε is the turbulence dissipation rate, m^2/s^3; β^* is a model constant; ω is the specific turbulent dissipation rate, 1/s; γ is the intermittency, -; σ_k is the turbulent Prandtl number, -; μ_{eff} is the effective viscosity, Pa·s; α_k is the inverse effective Prandtl number, -.

and radial momentum, and energy. The analysis thoroughly compares the terms of the budget equations, which are defined below. The generic form of the turbulence kinetic energy equation *k*, which consists of four terms, is presented as follows:

$$\mathrm{CONV}_k = \mathrm{PROD}_k - \mathrm{DISS}_k + \mathrm{DIFF}_k, \tag{7}$$

where: CONV – convection term, PROD – production term, DISS – dissipation term, DIFF – diffusion term. The subscript *k* means turbulence kinetic energy.

The choice of the turbulence model influences the *k* transport equation. In the post-processing stage, the convection, production, and dissipation terms can be directly calculated, while the diffusion term is determined as a closure term. Table 1 presents details of each term in Eq. (7) for analyzed turbulence models.

The generic form of the axial and radial momentum equations, which consists of four terms, is presented as follows:

$$\mathrm{CONV}_{M,i} = \mathrm{PRESS}_{M,i} + \mathrm{DIFF}_{M,i} + \mathrm{RS}_{M,i}, \tag{8}$$

where: CONV – convection term, PRESS – pressure term, DIFF – diffusion term, RS – Reynolds stress term. The subscript *M* means the momentum equation, and *i* indicates the axial (*y*) or radial (*x*) coordinate.

The axial and radial momentum equations are the same for all turbulence models. During the post-processing stage, the convection and pressure terms can be calculated quickly and directly. On the other hand, the diffusion term is obtained using a 'User-Defined Function' (UDF), a script that uses the Gauss-Ostrogradsky Theorem (see the Appendix). Lastly, the Reynolds stress term is determined as a closure term. The details of each term in the momentum budget can be found in Table 2.

The last one is the energy transport equation; it consists of three terms and is presented below in a generic form:

$$\mathrm{CONV}_E = \mathrm{DIFF}_E + \mathrm{TDIFF}_E, \tag{9}$$

where: CONV – convection term, DIFF – diffusion term, TDIFF – turbulent diffusion term. The subscript *E* means the energy equation.

The energy equation is the same for all turbulence models. The convection term is calculated directly in the post-process, but similarly to the momentum equation, the diffusion term is obtained by the UDF (see the Appendix). The turbulent diffusion term is determined as the closure term. Each term of the energy equation is presented in Table 3.

It is commonly seen in literature that budgets are typically prepared on a single line that is either parallel or normal to the heated wall [3,20–22,24–26,32]. The location at which the budget is calculated plays a crucial role. When the budget is calculated near the wall, the dissipation and diffusion terms in the TKE equation tend to dominate over the other terms, making it

Table 2. The momentum equation terms [28].

Term	*k–ε* RNG Kato-Launder, *k–ω* SST Kato-Launder, Intermittency transition	
	Axial	Radial
Convection	$\rho\left(U\frac{\partial V}{\partial x}+V\frac{\partial V}{\partial y}\right)$	$\rho\left(U\frac{\partial U}{\partial x}+V\frac{\partial U}{\partial y}\right)$
Pressure	$-\frac{\partial P}{\partial y}$	$-\frac{\partial P}{\partial x}$
Diffusion	$\frac{\partial}{\partial x}\left(\mu\frac{\partial V}{\partial x}\right)+\frac{\partial}{\partial y}\left(\mu\frac{\partial V}{\partial y}\right)$	$\frac{\partial}{\partial x}\left(\mu\frac{\partial U}{\partial x}\right)+\frac{\partial}{\partial y}\left(\mu\frac{\partial U}{\partial y}\right)$
Reynolds stress	$\frac{\partial}{\partial x}\left(\mu_t\left(\frac{\partial U}{\partial y}+\frac{\partial V}{\partial x}\right)\right)+\frac{\partial}{\partial y}\left(\mu_t 2\frac{\partial V}{\partial y}-\frac{2}{3}k\right)$	$\frac{\partial}{\partial x}\left(\mu_t 2\frac{\partial U}{\partial x}-\frac{2}{3}k\right)+\frac{\partial}{\partial y}\left(\mu_t\left(\frac{\partial U}{\partial y}+\frac{\partial V}{\partial x}\right)\right)$

where: ρ is the density, kg/m^3; U is the average radial velocity, m/s; V is the average axial velocity, m/s; x is the radial coordinate, m; y is the axial coordinate, m; μ is the dynamic viscosity, Pa·s; μ_t is the turbulent viscosity, Pa·s; P is the average static pressure, Pa.

Table 3. The turbulence kinetic energy equation terms [28].

Term	k–ε RNG Kato-Launder, k–ω SST Kato-Launder, Intermittency transition
Convection	$\rho\left(U\frac{\partial T}{\partial x}+V\frac{\partial T}{\partial y}\right)$
Diffusion	$\frac{\partial}{\partial x}\left(\frac{\lambda}{C_P}\frac{\partial T}{\partial x}\right)+\frac{\partial}{\partial y}\left(\frac{\lambda}{C_P}\frac{\partial T}{\partial y}\right)$
Turbulent diffusion (turbulent heat flux)	$\frac{\partial}{\partial x}\left(\frac{\mu_t}{\sigma_t}\frac{\partial T}{\partial x}\right)+\frac{\partial}{\partial y}\left(\frac{\mu_t}{\sigma_t}\frac{\partial T}{\partial y}\right)$

where: ρ is the density, kg/m^3; U is the average radial velocity, m/s; V is the average axial velocity, m/s; x is the radial coordinate, m; y is the axial coordinate, m; μ is the dynamic viscosity, Pa·s; μ_t is the turbulent viscosity, Pa·s; T – average static temperature, K; λ is the thermal conductivity, W/(m·K); C_P is specific heat capacity, J/(kg·K); σ_t is the turbulent Prandtl number, -.

challenging to observe the tendency of the convection and production terms, which are more significant away from the wall. The results of other studies [3,20–22,26] support this statement. In this paper, the authors analyze the budgets along vertical lines perpendicular to the heated wall to eliminate local value disturbances and observe the tendency of all equations terms. Each vertical line originates at the wall and extends 3 mm away. The endpoint of each line is selected to capture the region of maximum TKE values, located between 2 mm (0.1D) and 3 mm (0.15D) away from the heated wall, for both H/D = 2 and 6, and Re = 23 000. The results represent the integral value along the distance mentioned. Figure 5 shows the contour plot of the TKE values with the placement of its maximum, and velocity magnitude for k–ω SST Kato-Launder turbulence model. At H/D = 2 (Fig. 5(a)), the maximum occurs between x/D = 1.25 and 2, and approximately 0.1D from the wall. The literature results show similar region where the TKE maximum is located [9,14,23, 26,30]. At H/D = 6 (Fig. 5(c)) the maximum is located closer to the axis, between x/D = 0.9 and 1.4, and approximately the same distance from the heated wall (0.1D). Comparison between the TKE values (Figs. 5(a) and (c)) and velocity magnitude (Figs. 5(c) and (d)) for the same value of H/D suggests that the position of the maximal value of TKE is placed in the region of the strong interaction of the wall jet with the jet stream.

4. Results

4.1. Turbulence kinetic energy

Figure 6 compares the local turbulence kinetic energy (TKE) values on the line parallel to the heated wall between two geometrical configurations (H/D = 2 and 6) for three turbulence models. Analysis of the local k values for both geometrical configurations and all turbulence models shows that there is a maximum in their distribution, and further (x/D > 2.5) the values gradually decrease. Furthermore, it can be observed that the TKE values are relatively low in the stagnation region (x/D < 0.5), this statement is supported by the DNS results [20]. The high turbulence kinetic energy values at the stagnation point cause overprediction in the Nusselt number value. However, this problem can be resolved by incorporating the Kato-Launder limiter, which restricts the production of TKE at the stagnation point [10,27,33]. The results shown in Figs. 5 and 6 indicate a shift of relatively high values of k toward the stagnation point in the case of H/D = 6, which is consistent with the location of the highest values of the Nusselt number around the centerline, as suggested in [7]. On the other hand, at H/D = 2, the first Nusselt number maximum moved from the stagnation point and occurs at about x/D = 0.5. The relation between the local Nusselt number distribution of presented turbulence models is consistent with the relation between their TKE local values. If at the same radial position (x/D), the local TKE values obtained with the k–ε RNG Kato-Launder turbulence model are lower than values of TKE obtained with the intermittency transition turbulence model, and the same tendency is observed between their local Nusselt number values. The same pattern is observed across the entire range of x/D values for both geometrical configurations (except the near stagnation region at x/D < 0.5 and H/D = 6). It has been observed that the maximal values of the TKE are consistent with the second maximum of the Nusselt number distribution. It appears that other researchers have observed the occurrence of high values of TKE or turbulence intensity near the second Nusselt number maximum, as mentioned in [1,13,23,26, 32,34]. Interestingly, for a case of H/D = 2, the maximum value of k is observed ahead of the second maximum of the Nusselt number distribution and at H/D = 6, the maximum value of k is observed after the second maximum of the Nusselt number (for the k–ω SST Kato-Launder and Intermittency turbulence models). On the other hand, the k–ε RNG Kato-Launder turbulence model gives a results in which maximum in TKE values exists, but there is no second maximum in the Nusselt number (which is more consistent with experimental studies [35– 40]). Increasing the H/D value causes a shift of the TKE maximal values towards the stagnation point for all analyzed turbulence models. Additionally, the TKE values obtained with k–ω SST Kato-Launder and k–ε RNG Kato-Launder turbulence models decrease with an increase in the H/D parameter. However, the results obtained with the intermittency transition model exhibit a different tendency with an increase in the H/D parameter, leading to a rise in maximal value of TKE. The maximal values of TKE at H/D = 2 occur between x/D = 1.25 and x/D = 2.0, while for H/D = 6, they occur between x/D = 1.0 and x/D = 1.5. The analysis of the lowest H/D value confirms similarities in the local TKE distribution between all analyzed turbulence models. In the case of H/D = 6, the local TKE value distribution obtained with the k–ε RNG Kato-Launder turbulence model differs from the other two models of a constant offset.

4.2. Turbulence kinetic energy budget

In Fig. 7, a budget of turbulence kinetic energy, Eq. (7), is presented, and a few observations can be formulated. The TKE production and dissipation terms exhibit maximum positive and negative values in the case of k–ε RNG Kato-Launder and intermittency transition turbulence models, while the diffusion and dissipation terms dominate in the case of k–ω SST Kato-Launder turbulence model. These findings are consistent with an experimental study [3], which also reported maximum magnitudes of the production and dissipation terms. However, their maximal values in the experimental study are located near the x/D = 0.5,

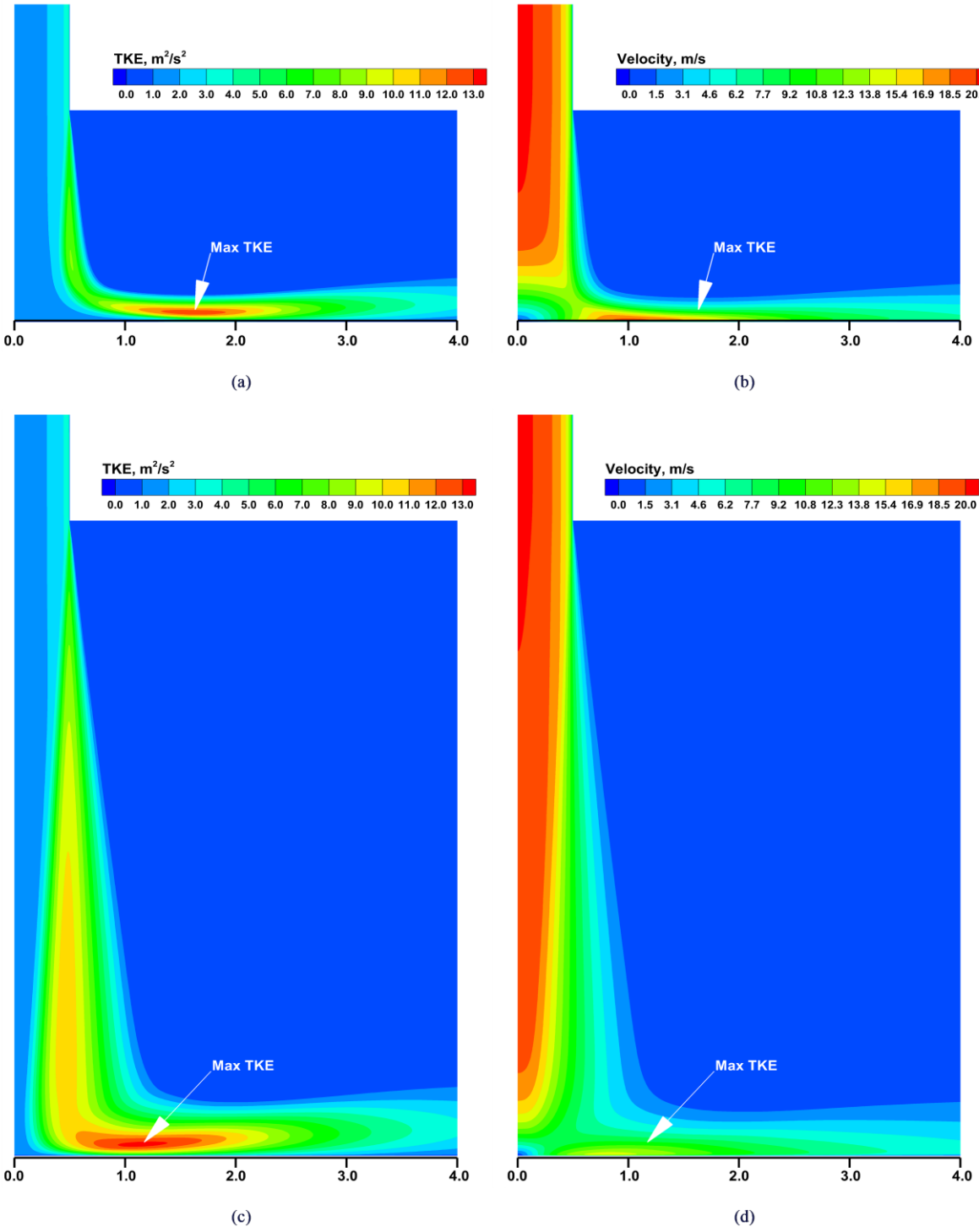

Fig. 5. Local values of TKE, with a position of its maximum, and local values of velocity magnitude. k–ω SST Kato-Launder turbulence model, Re = 23 000, D = 0.02 m. (a) TKE, H/D = 2. (b) Velocity magnitude, H/D = 2. (c) TKE, H/D = 6. (d) Velocity magnitude, H/D = 6.

which is closer to the stagnation point than the position of production and dissipation terms maximal values obtained by the presented numerical analysis. In the case of H/D = 2, the maxima and minima of all terms in the TKE equation are located between x/D = 1.0 and x/D = 2.0. A shifting towards the stagnation point can be seen for the second geometrical configuration (H/D = 6). The maxima and minima values are smaller than those of the H/D = 2 case. Another interesting observation is that the convection term changes sign, what was also reported in [3]. Other terms, such as production and diffusion, are always positive, while dissipation is negative. The research conducted through experimental and numerical (DNS) studies [9,20,22,41] has revealed that the production of turbulence kinetic energy is negative in the stagnation region, which is opposite to the values

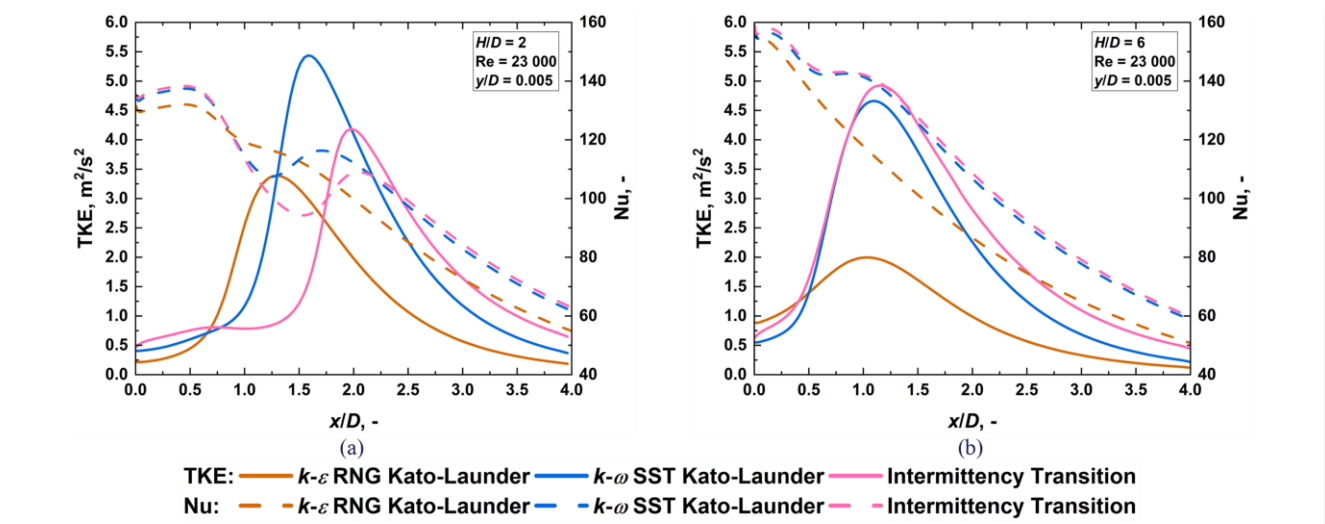

Fig. 6. Comparison of local values of TKE on a parallel to the heated wall line, between two geometrical configurations H/D values and Re = 23 000, for various turbulence models (a) H/D = 2; (b) H/D = 6. Re = 23 000.

predicted by RANS turbulence models. According to the results of the RANS, the production of turbulence kinetic energy is always positive, indicating the energy transfer from the mean flow to the eddies. As mentioned in [9], this challenges the RANS and LES models. The relatively low TKE production values in the stagnation region are due to the Kato-Launder limiter [10]. The production term of TKE (Fig. 7) and local values of TKE (Fig. 6) exhibit a similar tendency, location of their maxima correspond to each other. The maximum values of the production term correspond to the second maximum value of the local Nusselt number. When the H/D parameter is equal to 2, all turbulence models exhibit similar behavior in terms of the TKE production. The analysis of the convection term reveals a positive value near the stagnation point, and its sign change near the location of the first and second local Nusselt number maxima. In addition, the convection term's lowest value corresponds with the local Nusselt number minimum, while its maximal value occurs behind the secondary Nusselt number maximum. Moreover, the k–ε RNG Kato-Launder turbulence model results show a different behavior in the second geometrical configuration (H/D = 6), as presented in Fig. 7(f). The convection term in this configuration has its local minima and maxima, but it is always positive. This observation is particularly interesting as the k–ε RNG Kato-Launder turbulence model does not show a false secondary Nusselt number maximum in this geometrical configuration. Hence, it suggests a connection between the Nusselt number distribution and the convection term of the turbulence kinetic energy budged. The shape of the dissipation term mirrors the production term, what has been noticed in [9]. The diffusion maximum and dissipation minimum are observed near the Nusselt number second maximum. Compared to the other two models, the k–ε RNG Kato-Launder turbulence model exhibits flatter and lower absolute values for these two terms. All terms of the turbulence kinetic energy equation exhibit higher absolute values for H/D = 2 than for H/D = 6. The tendency of all terms is quite similar for the k–ω SST Kato-Launder and intermittency transition turbulence models across both geometrical configurations (Fig. 7(a)–(d)). The k–ε RNG Kato-Launder turbulence model results show differences in trend between H/D = 2 and H/D = 6 cases. In the first geometrical configuration, the shape is similar to the other two turbulence models, but in the second case the shape does not exhibit second maximum and all terms except dissipation are positive.

4.3. Momentum budget

The momentum equation budget, Eq. (8), is considered separately for the axial and radial coordinates. Figures 8 and 9 show the radial and axial components of the momentum budget, respectively. The characteristic of all terms in the momentum equation is similar for all analyzed turbulence models and both geometrical configurations. In the case of the radial (x) component, the convection and pressure terms are the dominant ones, while the Reynolds stress term takes the lowest values. Comparing the H/D = 6 case with the H/D = 2 shows that features of all terms' are similar, but the values are significantly lower in the case of H/D = 6. The analysis of the axial momentum component budget reveals some similarities to that of the radial component. The convection and pressure terms are also dominant, whereas the Reynolds stress term is larger than the same term in the case of the radial momentum equation. The diffusion term is almost negligible, which aligns with the findings presented in [22]. There is a significant difference in the characteristics of axial (y) momentum equation terms between H/D = 2 and H/D = 6, especially visible in the stagnation region x/D < 1.0. Almost whole turbulence kinetic energy is concentrated in this region. With an increase in the x/D parameter, especially in the range x/D > 2.0, all terms tend to approach 0. On the basis of the analysis of all cases, the convection and pressure terms exhibit a mirror-like shape. In the case of the radial (x) momentum, the pressure term is always positive, the diffusion and Reynolds stress terms are always negative, and the convection term changes sign. On the other hand, the pressure term is always negative for the axial (y) momentum equation, while the convection and Reynolds stress terms are positive. The almost negligible diffusion term changes sign near x/D = 2.5. The large absolute values of the convection

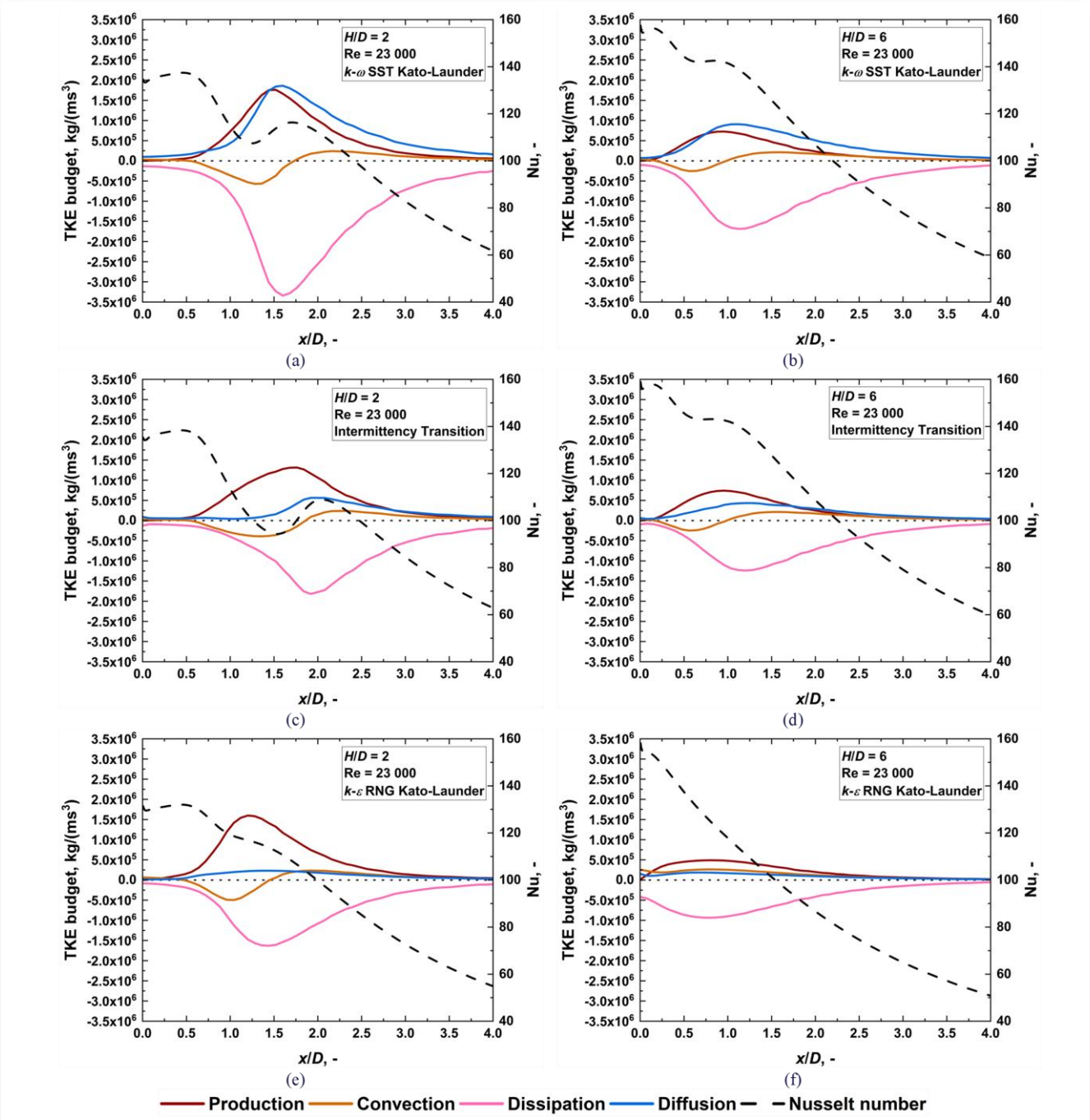

Fig. 7. Comparison of TKE budget, between two geometrical configurations (H/D values 2 and 6) and for various turbulence models. (a) k–ω SST Kato-Launder, H/D = 2; (b) k–ω SST Kato-Launder, H/D = 6; (c) intermittency transition, H/D = 2; (d) intermittency transition, H/D = 6; (e) k–ε RNG Kato-Launder, H/D = 2; (f) k–ε RNG Kato-Launder, H/D = 6; Re = 23 000.

and pressure terms in both components of the momentum equation clearly mark the limit of the stagnation region at $x/D \approx 1.0$. The minimum and maximum values of the pressure and convection terms correspond to the first maximum value of the local Nusselt number. A link between radial (x) pressure gradient and the first Nusselt number maximum has been mentioned in [11]. The maximum and minimum values of the pressure and convection terms are closer to the stagnation point at H/D = 6 ($x/D \approx 0.25$) than at H/D = 2 ($x/D \approx 0.5$). This is also reflected in the shift of the first maximum of the local Nusselt number towards the jet axis. In contrast to the budget of TKE, it is hard to see any relation between the sign change in the convection term of the radial momentum component and the local Nusselt number distribution in this case. For example, at H/D = 2, the sign change occurs before the local minimum in the Nusselt number and behind the second Nusselt number maximum at H/D = 6. The convection and pressure terms of the axial momentum equation component show values that are almost constant near the axis. A similar observation on the constant value of the convection term can be found in [3]. The Reynolds stress term in the axial momentum component equation takes higher values for the k–ε RNG Kato-Launder turbulence model at the stagnation point than the other two models in the case of H/D = 6.

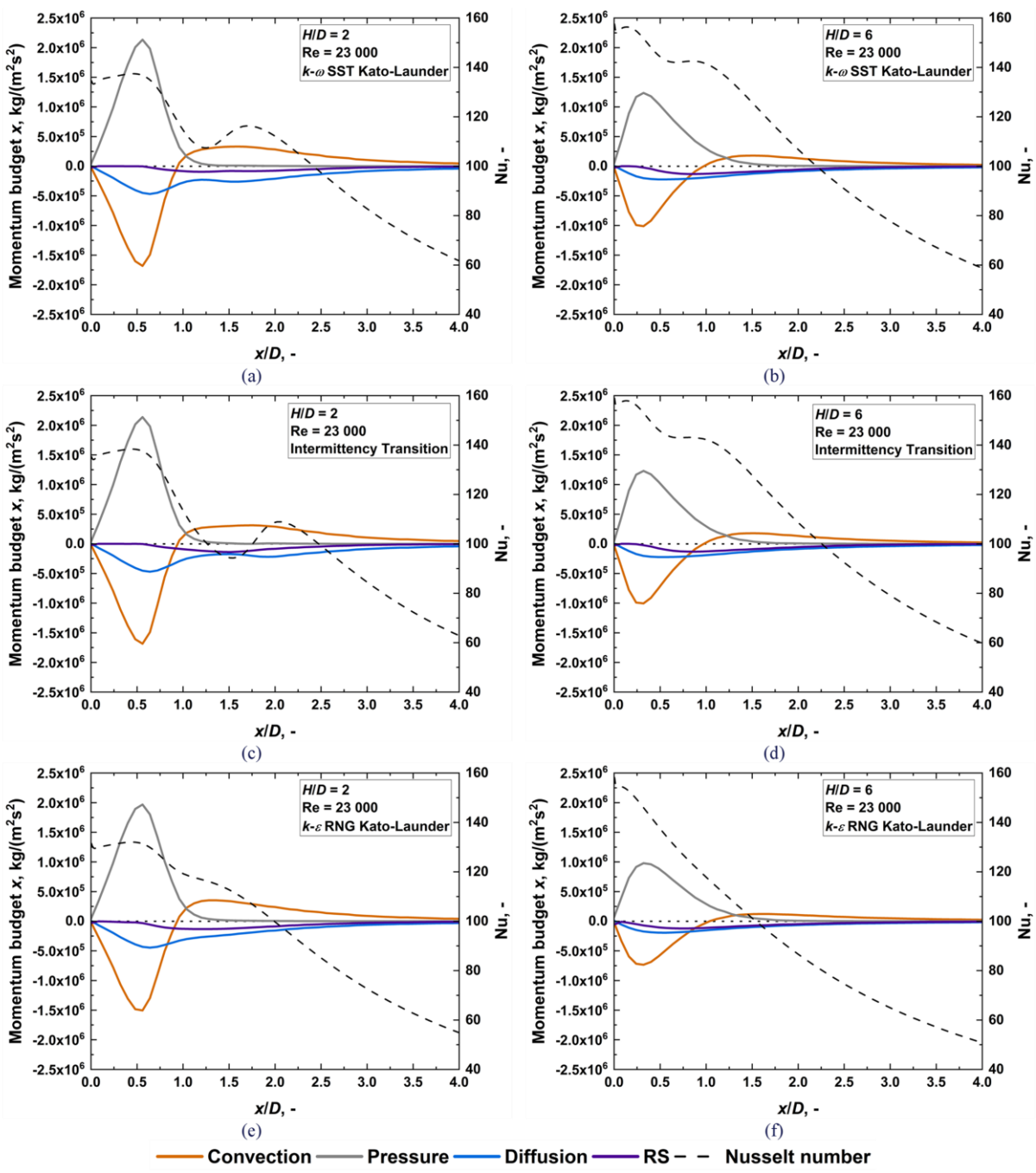

Fig. 8. Comparison of radial momentum budget, between two geometrical configurations (H/D values 2 and 6) and for various turbulence models. (a) k–ω SST Kato-Launder, H/D = 2; (b) k–ω SST Kato-Launder, H/D = 6; (c) itermittency transition, H/D = 2, (d) intermittency transition, H/D = 6; (e) k–ε RNG Kato-Launder, H/D = 2; (f) k–ε RNG Kato-Launder, H/D = 6; Re = 23 000.

4.4. Energy budget

The last budget is related to the energy equation, Eq. (9), and presented in Fig. 10. It was observed that the shapes of all terms remain similar, regardless of the turbulence model used and the geometrical configurations. However, there was one exception to this observation, which is presented in Fig. 10(f). The diffusion term is always positive for all cases, and the convection and turbulent diffusion terms are always negative. The crossing point between convection and turbulent diffusion terms is very characteristic. This point occurs prior to the second Nusselt number maximum. In Fig. 10(f), which presents the results of the k–ε RNG Kato-Launder turbulence model at H/D = 6, the crossing point is located far from the stagnation point at x/D > 3.0, and the curves tend to converge. The observation is particularly interesting because, for this geometrical configuration and this specific turbulence model, the second Nusselt number maximum does not exist. This raises the possibility of a potential correlation between these two terms and the distribution of the

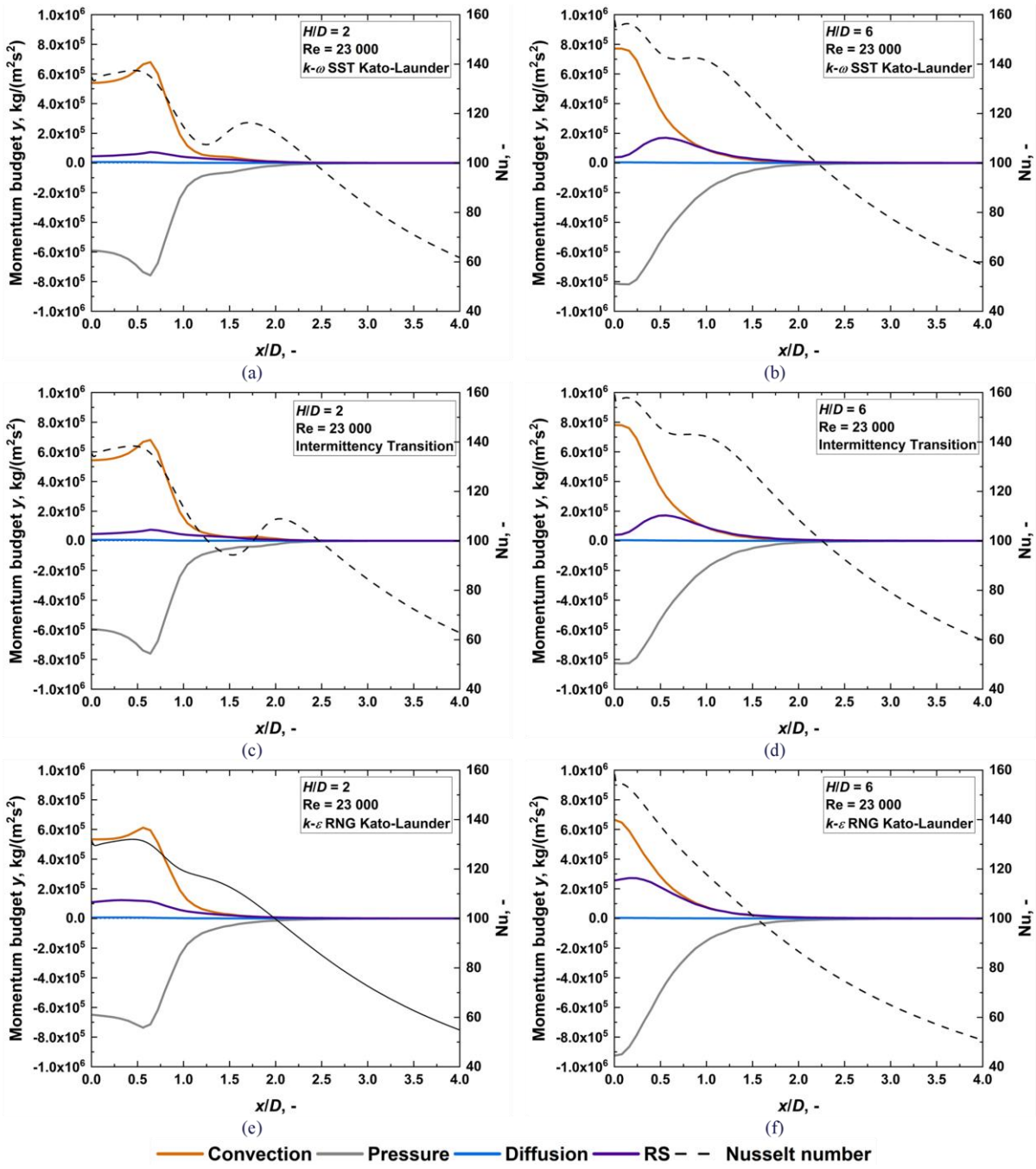

Fig. 9. Comparison of axial momentum budget, between two geometrical configurations (H/D values 2 and 6) and for various turbulence models. (a) k–ω SST Kato-Launder, H/D = 2; (b) k–ω SST Kato-Launder, H/D = 6; (c) intermittency transition, H/D = 2; (d) intermittency transition, H/D = 6; (e) k–ε RNG Kato-Launder, H/D = 2; (f) k–ε RNG Kato-Launder, H/D = 6; Re = 23 000.

local Nusselt number. The convection and diffusion terms dominate in the stagnation region, while the turbulent diffusion term is close to 0. As the value of x/D increases, the role of turbulent diffusion becomes more significant, while the impact of the convection term decreases. This tendency is clear, especially outside the stagnation region $x/D > 1.0$. In the k–ω SST Kato-Launder and intermittency transition turbulence models, the diffusion term shows local minima and maxima, which correspond to the distribution of the local Nusselt number, but in the k–ε RNG Kato-Launder turbulence model the diffusion term does not exhibit the extrema. The tendency of all terms is similar for the k–ω SST Kato-Launder and intermittency transition turbulence models but differs for the k–ε RNG Kato-Launder turbulence model. The absolute values of all terms are lower at H/D = 6 compared to H/D = 2. It has been observed that the k–ω SST Kato-Launder and intermittency transition turbulence models exhibit local minima and maxima in the convection and turbulent diffusion terms at H/D = 2. This corresponds to the second Nusselt number maximum. However, at H/D = 6, the maxima and minima are small or non-existent. All terms have almost constant values near the axis at $x/D < 0.5$.

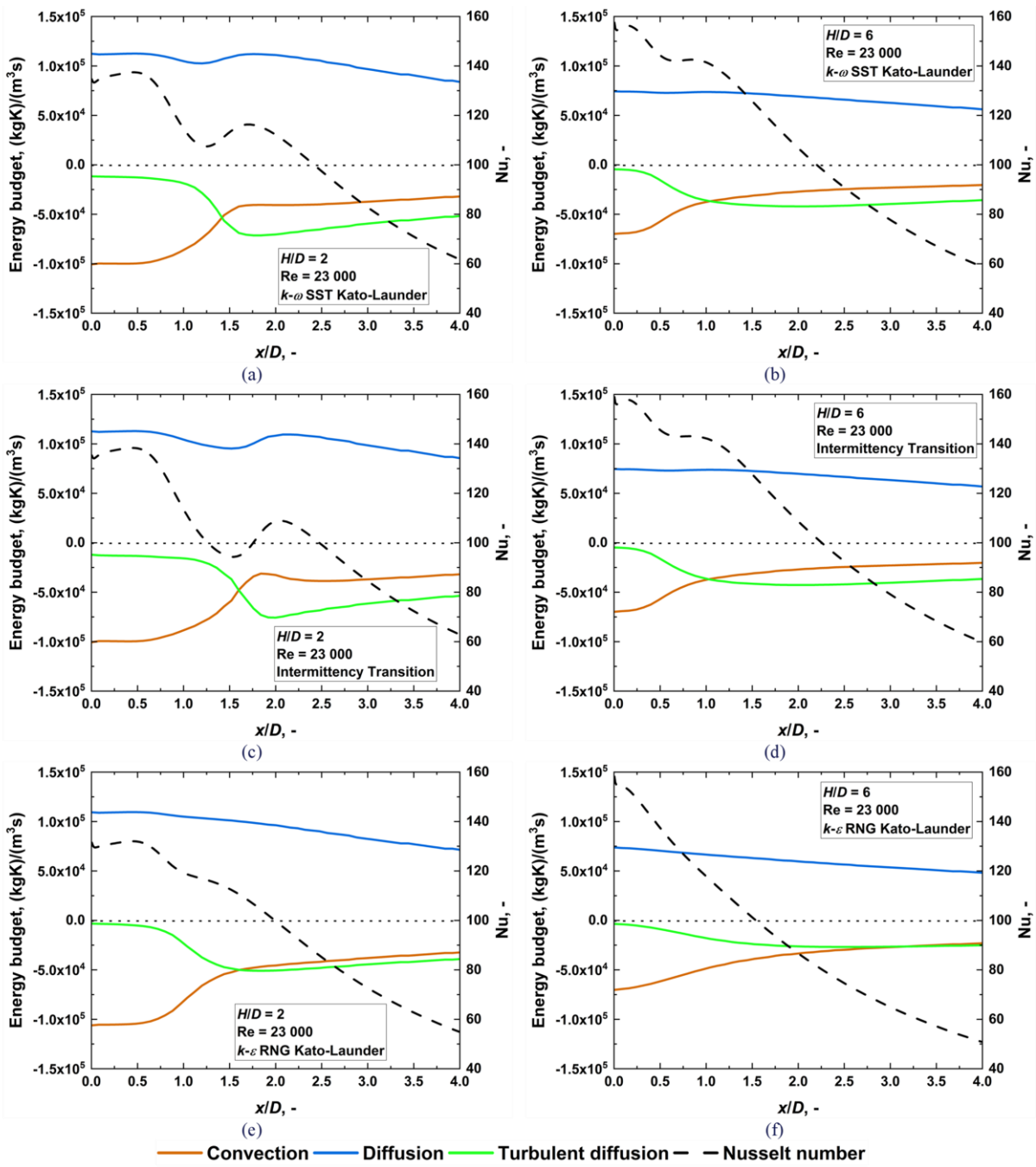

Fig. 10. Comparison of energy budget, between two geometrical configurations (H/D values 2 and 6) and for various turbulence models. (a) k–ω SST Kato-Launder, H/D = 2; (b) k–ω SST Kato-Launder, H/D = 6; (c) Intermittency transition, H/D = 2; (d) intermittency transition, H/D = 6; (e) k–ε RNG Kato-Launder, H/D = 2; (f) k–ε RNG Kato-Launder, H/D = 6. Re = 23 000.

5. Summary

The publication presented a budget of the turbulence kinetic energy, momentum, and energy equations together with the local values of TKE in the case of turbulent round jet impingement. The comparative analysis was prepared for one Reynolds number (Re = 23 000), three selected turbulence models, and two geometrical configurations (H/D = 2 and 6). This analysis might help identify the essential transport phenomena in the RANS numerical modeling of turbulent heat transport. The study also includes comparison of the results of transport equation budgets with the local Nusselt number values, which might provide insights into the relation between transport equation terms and the local Nusselt number distribution. This study can be used for further analysis and considerations, and in the future, it can be enriched with more formal analysis such as the curve sketching technique. This method would allow for a more precise determination of minima and maxima, inflection points for budgets, and the local Nusselt number. Some general conclusions from this study are presented below:

TKE and TKE budget

- Maximal values of TKE are consistent with the location of the second Nusselt number maximum, at H/D = 2 occurring between x/D = 1.25 and 2.0, while at H/D = 6, it is between x/D = 1.0 and 1.5.
- In the TKE budget, production and dissipation terms dominate in the k–ε RNG Kato-Launder and intermittency transition turbulence models. In contrast, the diffusion and dissipation terms dominate in the k–ω SST Kato-Launder turbulence model.
- The maxima and minima of all terms in the TKE budgets can be found between x/D = 1.0 and 2.0 at lower geometrical configuration (H/D = 2). An increase in the H/D value shifts those maxima and minima towards the stagnation point.
- The maximal values of the production term in the TKE budget correspond to the maximal values of the local Nusselt number distribution.

Momentum budget

- The behavior of all terms in the momentum equation is similar for all analyzed turbulence models for both geometrical configurations.
- The convection and pressure terms in the radial and axial momentum equations dominate. The diffusion term in the axial momentum equation is almost negligible.
- The large absolute values of the convection and pressure terms in the equations of both momentum components identify the stagnation region's limit at $x/D \approx 1.0$.
- The minimum and maximum values of the pressure and convection terms in the momentum budgets correspond to the first Nusselt number maximum.

Energy budget

- In the energy equation budget, the convection and diffusion terms dominate in the stagnation region.
- The crossing point between the convection and turbulent diffusion terms in the energy equation budget coincides with the second Nusselt number maximum for the k–ω SST Kato-Launder and intermittency transition turbulence models. This crossing point does not occur for the k–ε RNG Kato-Launder turbulence model at the H/D = 6 case, which corresponds to a lack of secondary Nusselt number maximum.

General

- The trend of the transport equation budget for the k–ε RNG Kato-Launder turbulence model at the H/D = 6 case differs from the other two presented turbulence models.
- The convection term is the only term in TKE and radial momentum budget that changes its sign across the x/D parameter.
- The analysis of all transport equation budgets shows that in the H/D = 6 case, the values of all terms are lower than in the H/D = 2 case, maybe with one exception for the axial momentum budget, where they are higher at the stagnation point.

Guideline

- None of the presented budgets alone describes the Nusselt number distribution. Each equation contributes to it, so only together they properly describe the physics of this phenomenon. Moreover, none of the equation terms can be neglected (even if they are relatively small compared to other terms), and each of them influences the heat transfer.
- In the boundary layer, molecular diffusion transports the heat from the wall, and then in the outer layer the convection mechanism plays a significant role in the heat transfer mechanism. Those two terms are the most important ones in the energy equation, which creates the general shape of the Nusselt number distribution and its high values. Moreover, the convection term is responsible for the first Nusselt number maximum. However, convection and molecular diffusion terms alone cannot describe the second Nusselt number maximum, for which the turbulent diffusion term is responsible. Because of that, the energy equation budget might seem to be the most important one to analyze, but both terms responsible for Nusselt number maxima – convection (first one) and turbulent diffusion (second one) are described by other transport equations – momentum and TKE equations, respectively. Therefore, the focus should be on the momentum (axial and radial) and the turbulence kinetic energy budgets.
- Jet's movement toward the wall is represented by the convective term in the momentum budget, then it impinged on the wall, which causes the increase in the pressure due to slowing down of the fluid. The high pressure in the stagnation region forced radial movement of the fluid, so it can be said that the pressure term of the momentum budget contributes to the development of the flow. Both phenomena (convection term in axial momentum budget supported by the pressure term in radial momentum budget) determined the existence of the first Nusselt number maximum.
- The second Nusselt number maximum represents the development of a turbulent boundary layer in a wall jet and its interaction with the jet stream. Proper modeling of turbulence (like TKE equation terms) is crucial to adequately describe the Nusselt number distribution in a whole range, which is why various turbulence models describe the Nusselt number distribution differently.
- Both the k–ω SST Kato-Launder and the intermittency transition turbulence models tend to generate a secondary Nusselt number maximum. For low values of H/D (H/D = 2), it is the real (observed in the experimental studies), but for high values of H/D (H/D = 6) is the fake one (not observed in the experimental studies). On the other hand, the k–ε RNG Kato-Launder turbulence model does not tend to generate a secondary Nusselt

number maximum, and it is a better option for higher H/D values.

- The selection of the best turbulence model that describes the heat transfer of the impingement jet in a range of various Reynolds numbers and values of H/D cannot be made on the presented study. It only supports the recommendations of the previous analysis. The source of the difference is probably in the dissipation and diffusion terms of the TKE equation. Further research should also include the ε/ω transport equations budgets.

Acknowledgements

This research was supported by the Ministry of Education and Science.

Appendix

In general, the diffusion term of any variable in finite volume method can be calculated by the equation:

$$\frac{\partial}{\partial x}\left(\Gamma\frac{\partial\phi}{\partial x}\right)+\frac{\partial}{\partial y}\left(\Gamma\frac{\partial\phi}{\partial y}\right)=\frac{1}{V_c}\sum_f \Gamma_f \frac{\phi_c-\phi_{nc}}{d_{nc}}A_f\overrightarrow{n_f}, \qquad (10)$$

where: ϕ is the variable (e.g.: temperature, velocity, etc.); Γ is the diffusion coefficient; V_c is the cell volume; A_f is the face area; $\overrightarrow{n_f}$ is the face unit normal vector; d_{nc} is the distance between the cell centroids; ϕ_c is the variable value at the cell center; ϕ_{nc} is the variable value at the neighbor cell center; subscript f indicates cell face.

Figure 11 shows a graphical representation of all variables in that equation:

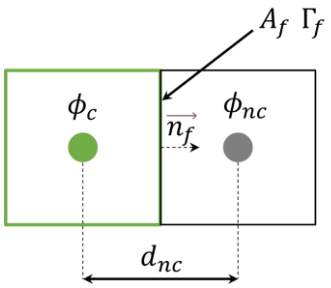

Fig. 11. Graphical representation of all variables in Eq. (10).

The implementation of Eq. (10) for 2D axisymmetric model, using built-in UDF functions, such as connectivity macros [42], for the energy equation, the diffusion term is presented below. The code must be compiled first and then used in the Ansys Fluent model.

```
#include "udf.h"
#include "sg.h"

DEFINE_ON_DEMAND(on_demand_energy_diffusion_term){
Domain *d;
Thread *t;
cell_t c;
d = Get_Domain(1);
real xc[ND_ND];  /* cell centroid */
real xf[ND_ND]; /* face centroid */

thread_loop_c(t,d){

/* loop through all cells in the model */
begin_c_loop(c,t){

/* face variables */
face_t f;
Thread *tf;
int n;
C_CENTROID(xc,c,t);     /* get cell centroid data */
real phi_f = 0;         /* values at the face center */
real diff = 0;          /* diffusion term */
/* cell, face connectivity macros defined in [42] */
real A[2];
real ds;
real es[2];
real A_by_es;
real dr0[2];
real dr1[2];

/* loop through all faces in the cell */
c_face_loop(c, t, n){

    f = C_FACE(c,t,n);
    tf = C_FACE_THREAD(c,t,n);
    F_CENTROID(xf,f,tf); /* get face centroid data */
```

```
    if (BOUNDARY_FACE_THREAD_P(tf)){ /* if face is the boundary face */

        BOUNDARY_FACE_GEOMETRY(f,tf,A,ds,es,A_by_es,dr0);
        phi_f = 0.0242/1006.43; /* thermal conductivity/Cp */

        phi_f = phi_f*(C_T(F_C0(f,tf),THREAD_T0(tf))-F_T(F_C0(f,tf),THREAD_T0(tf)))*A_by_es/ds;
    }
    else{   /* if face is an interior face */

        INTERIOR_FACE_GEOMETRY(f,tf,A,ds,es,A_by_es,dr0,dr1);
        phi_f = 0.0242/1006.43; /* thermal conductivity/Cp */

        phi_f = phi_f*(C_T(F_C0(f,tf),THREAD_T0(tf))-C_T(F_C1(f,tf),THREAD_T1(tf)))
        *A_by_es/ds;
    }

    if (THREAD_TYPE(tf) == THREAD_F_AXIS){ /* if axis */
        diff  -= 0;
    }
    else{

        /* phi_f * face normal */
        phi_f = phi_f * (xf[0] - xc[0])/sqrt((xf[0] - xc[0])*(xf[0] - xc[0])+(xf[1] - xc[1])*(xf[1] - xc[1]))
        + phi_f * (xf[1] - xc[1])/sqrt((xf[0] - xc[0])*(xf[0] - xc[0])+(xf[1] - xc[1])*(xf[1] - xc[1]));

        diff += -phi_f/xf[1]; /* scale face value by face center radius and sum */
    }
}

/* The diffusion term for a cell (for 2D axisymmetric case, volume must be scaled by radius) */
C_UDMI(c,t,0) = xc[1] * diff / C_VOLUME(c,t);

}
end_c_loop(c,t)
}
}
```

References

[1] Barbosa, F.V., Teixeira, S.F.C.F., & Teixeira, J.C.F. (2023). Convection from multiple air jet impingement – A review. *Applied Thermal Engineering*, 218, 119307. doi: 10.1016/j.applthermaleng.2022.119307

[2] Chitsazan, A., Klepp, G.,& Glasmacher, B. (2021). Numerical prediction of the second peak in the Nusselt number distribution from an impinging round jet. *International Journal of Heat and Technology*, 39(4), 1243–1252. doi: 10.18280/ijht.390422

[3] Alekseenko, S.V., Bilsky, A.V., Dulin, V.M., & Markovich, D.M. (2007). Experimental study of an impinging jet with different swirl rates. *International Journal of Heat and Fluid Flow*, 28(6), 1340–1359. doi: 10.1016/j.ijheatfluidflow.2007.05.011

[4] Magagnato, F., Secchi, F., Forooghi, P., Straub, S., & Frohnapfel, B. (2021). DNS of turbulent heat transfer in impinging jets at different Reynolds and Prandtl numbers. *World Congress in Computational Mechanics and ECCOMAS Congress*, 300, 1–12. doi: 10.23967/wccm-eccomas.2020.299

[5] van Hout, R., Rinsky, V., & Grobman, Y.G. (2018). Experimental study of a round jet impinging on a flat surface: Flow field and vortex characteristics in the wall jet. *International Journal of Heat and Fluid Flow*, 70, 41–58. doi: 10.1016/j.ijheatfluidflow.2018.01.010

[6] Menzler, J. E., Klusmann, M., Wulfmeier, M., Büschgens, D., & Pfeifer, H. (2023). Simulation of gas jet impingement cooling in continuous heat treatment lines with the ANSYS GEKO turbulence model. *HTM - Journal of Heat Treatment and Materials*, 78(2), 91–104. doi: 10.1515/htm-2022-1042

[7] Ahmed, Z.U., Al-Abdeli, Y. M., & Guzzomi, F.G. (2017). Flow field and thermal behaviour in swirling and non-swirling turbulent impinging jets. *International Journal of Thermal Sciences*, 114, 241–256. doi: 10.1016/j.ijthermalsci.2016.12.013

[8] Korinek, T., Frana, K., Hujer, J., & Škarohlíd, J. (2022). Influence of local grid refinement on prediction of impinging jet heat transfer using Scale-Resolving-Simulation methods. *Case Studies in Thermal Engineering*, 36, 102159. doi: 10.1016/j.csite.2022.102159

[9] Domino, S.P., & Wenzel, E.A. (2023). A direct numerical simulation study for confined non-isothermal jet impingement at moderate nozzle-to-plate distances: Capturing jet-to-ambient density effects. *International Journal of Heat and Mass Transfer*, 211, 124168. doi: 10.1016/j.ijheatmasstransfer.2023.124168

[10] Huang, H., Sun, T., Zhang, G., Li, D., & Wei, H. (2019). Evaluation of a developed SST k–ω turbulence model for the prediction of turbulent slot jet impingement heat transfer. *International Journal of Heat and Mass Transfer*, 139, 700–712. doi: 10.1016/j.ijheatmasstransfer.2019.05.058

[11] Zhang, G., Huang, H., Sun, T., Li, N., Zhou, B., & Sun, Z. (2019). Analysis of the performance of a new developed shear stress transport model in a turbulent impinging jet flow. *Physics of Fluids*, 31(11), 115110. doi: 10.1063/1.5118675

[12] Huang, H., Sun, T., Li, N., & Zhang, G. (2022). Sensitization of the modified SST model to the swirling and curvature for turbulent

impinging jet heat transfer. *International Journal of Heat and Mass Transfer*, 182, 121980. doi: 10.1016/j.ijheatmasstransfer.2021.121980

[13] Huang, H., Sun, T., Zhang, G., Liu, M., & Zhou, B. (2021). The effects of rough surfaces on heat transfer and flow structures for turbulent round jet impingement. *International Journal of Thermal Sciences*, 166, 106982. doi: 10.1016/j.ijthermalsci.2021.106982

[14] Kaewbumrung, M., & Plengsa-Ard, C. (2023). Numerical simulation of jet impingement relaminarization using nonlinear eddy viscosity turbulence models. *Engineering Applications of Computational Fluid Mechanics*, 17(1), 2162132. doi: 10.1080/19942060.2022.2162132

[15] Siddique, M.U., Syed, A., Khan, S.A., & Meyer, J.P. (2022). On numerical investigation of heat transfer augmentation of flat target surface under impingement of steady air jet for varying heat flux boundary condition. *Journal of Thermal Analysis and Calorimetry*, 147(6), 4325–4337. doi: 10.1007/s10973-021-10785-4

[16] Kumar, A., Yogi, K., & Prabhu, S.V. (2023). Experimental and analytical study on local heat transfer distribution between smooth flat plate and free surface impinging jet from a circular straight pipe nozzle. *International Journal of Heat and Mass Transfer*, 207, 124004. doi: 10.1016/j.ijheatmasstransfer.2023.124004

[17] Hussain, L., Khan, M.M., Masud, M., Ahmed, F., Rehman, Z., Amanowicz, Ł., & Rajski, K. (2021). Heat transfer augmentation through different jet impingement techniques: A state-of-the-art review. *Energies*, 14(20), 6458. doi: 10.3390/en14206458

[18] Wai, O.J., Gunnasegaran, P., & Hasini, H. (2022). A Review on Experimental and Numerical Investigations of Jet Impingement Cooling Performance with Nanofluids. *Micromachines*, 13(12), 2059. doi: 10.3390/mi13122059

[19] Plant, R.D., Friedman, J., & Saghir, M.Z. (2023). A review of jet impingement cooling. *International Journal of Thermofluids*, 17, 100312. doi: 10.1016/j.ijft.2023.100312

[20] Ries, F., Li, Y., Rißmann, M., Klingenberg, D., Nishad, K., Bohm, B., Dreizler, A., Janicka, J., & Sadiki, A. (2018). Database of near-wall turbulent flow properties of a jet impinging on a solid surface under different inclination angles. *Fluids*, 3(1), 1–22. doi: 10.3390/fluids3010005

[21] Ries, F., Li, Y., Klingenberg, D., Nishad, K., Janicka, J., & Sadiki, A. (2018). Near-wall thermal processes in an inclined impinging jet: analysis of heat transport and entropy generation mechanisms. *Energies*, 11(6), 1354. doi: 10.3390/en11061354

[22] Nishino, K., Samada, M., Kasuya, K., & Torii, K. (1996). Turbulence statistics in the stagnation region of an axisymmetric impinging jet flow. *International Journal of Heat and Fluid Flow*, 17(3), 193–201. doi: 10.1016/0142-727X(96)00040-9

[23] Kura, T., Fornalik-Wajs, E., Wajs, J., & Kenjeres, S. (2019). Heat transfer intensification by jet impingement – numerical analysis using RANS approach. *E3S Web of Conferences*, 108, 01025. doi: 10.1051/e3sconf/201910801025

[24] Kura, T., Fornalik-Wajs, E., Wajs, J., & Kenjeres, S. (2018). Local Nusselt number evaluation in the case of jet impingement. *Journal of Physics: Conference Series*, 1101(1), 012018. doi: 10.1088/1742-6596/1101/1/012018

[25] Kura, T., Fornalik-Wajs, E., Wajs, J., & Kenjeres, S. (2018). Turbulence models impact on the flow and thermal analyses of jet impingement. *MATEC Web of Conferences*, 240, 01016. doi: 10.1051/matecconf/201824001016

[26] Kura, T., Wajs, J., Fornalik-Wajs, E., Kenjeres, S., & Gurgul, S. (2020). Thermal and Hydrodynamic Phenomena in the Stagnation Zone—Impact of the Inlet Turbulence Characteristics on the Numerical Analyses. *Energies*, 14(1), 105. doi: 10.3390/en14010105

[27] Gurgul, S., & Fornalik-Wajs, E. (2023). On the Measure of the Heat Transfer Performance of RANS Turbulence Models in Single Round Jet Impingement. *Energies*, 16(21), 7236. doi: 10.3390/en16217236

[28] *Ansys Fluent, Release 18.1: Theory Guide*. ANSYS Inc., 2018.

[29] Gurgul, S., & Fornalik-Wajs, E. (2023). Turbulent single round jet impingement – numerical data collection, V1, *AGH University of Krakow*. doi: 10.58032/AGH/2SRV8O

[30] Uddin, N., Neumann, S.O., & Weigand, B. (2013). LES simulations of an impinging jet: On the origin of the second peak in the Nusselt number distribution. *International Journal of Heat and Mass Transfer*, 57(1), 356–368. doi: 10.1016/j.ijheatmasstransfer.2012.10.052

[31] Hadžiabdić, M., & Hanjalić, K. (2008). Vortical structures and heat transfer in a round impinging jet. *Journal of Fluid Mechanics*, 596, 221–260. doi: 10.1017/S002211200700955X

[32] Hattori, H., & Nagano, Y. (2004). Direct numerical simulation of turbulent heat transfer in plane impinging jet. *International Journal of Heat and Fluid Flow*, 25(5), 749–758. doi: 10.1016/j.ijheatfluidflow.2004.05.004

[33] Wienand, J., Riedelsheimer, A., & Weigand, B. (2017). Numerical study of a turbulent impinging jet for different jet-to-plate distances using two-equation turbulence models. *European Journal of Mechanics - B/Fluids*, 61, 210–217. doi: 10.1016/j.euromechflu.2016.09.008

[34] Zuckerman, N., & Lior, N. (2005). Impingement Heat Transfer: Correlations and Numerical Modeling. *Journal of Heat Transfer*, 127(5), 544–552. doi: 10.1115/1.1861921

[35] Katti, V., & Prabhu, S.V. (2008). Experimental study and theoretical analysis of local heat transfer distribution between smooth flat surface and impinging air jet from a circular straight pipe nozzle. *International Journal of Heat and Mass Transfer*, 51(17–18), 4480–4495. doi: 10.1016/j.ijheatmasstransfer.2007.12.024

[36] Gao, N., Sun, H., & Ewing, D. (2003). Heat transfer to impinging round jets with triangular tabs. *International Journal of Heat and Mass Transfer*, 46(14), 2557–2569. doi: 10.1016/S0017-9310(03)00034-6

[37] Baughn, J.W., Hechanova, A.E., & Yan, X. (1991). An experimental study of entrainment effects on the heat transfer from a flat surface to a heated circular impinging jet. *Journal of Heat Transfer*, 113(4), 1023–1025. doi: 10.1115/1.2911197

[38] Baughn, J. W., & Shimizu, S. (1989). Heat transfer Measurements from a surface with uniform heat flux and an impinging jet. *Journal of Heat Transfer*, 111(4), 1096–1098. doi: 10.1115/1.3250776

[39] Lytle, D., & Webb, B. (1994). Air jet impingement heat transfer at low nozzle-plate spacings. *International Journal of Heat and Mass Transfer*, 37(12), 1687–1697. doi: 10.1016/0017-9310(94)90059-0

[40] Lee, D.H., Song, J., & Jo, M.C. (2004). The effects of nozzle diameter on impinging jet heat transfer and fluid flow. *Journal of Heat Transfer*, 126(4), 554–557. doi: 10.1115/1.1777583

[41] Tummers, M.J., Jacobse, J., & Voorbrood, S.G.J. (2011). Turbulent flow in the near field of a round impinging jet. *International Journal of Heat and Mass Transfer*, 54(23–24), 4939–4948. doi: 10.1016/j.ijheatmasstransfer.2011.07.007

[42] *Ansys Fluent, Release 18.1: ANSYS Fluent UDF Manual*. ANSYS Inc., 2018.